J. Marine Sci. Appl. (2011) 10: 495-501
DOI: 10.1007/s11804-011-1097-7

The Representation of a Broadband Vector Field

Qunyan Ren[1*], Jean Pierre Hermand[1] and Shengchun Piao[2]

1. Environmental Hydroacoustics Laboratory (EHL), Faculty of Applied Sciences/Polytechnic School, Université libre de Bruxelles (U.L.B.), 1050 Belgium
2. National Key Laboratory of Underwater Acoustic Technology, Harbin Engineering University (HEU), Harbin 150001, China

Abstract: Compared to a scalar pressure sensor, a vector sensor can provide a higher signal-to-noise ratio (SNR) signal and more detailed information on the sound field. Study on vector sensors and their applications have become a hot topic. Research on the representation of a vector field is highly relevant for extending the scope of vector sensor technology. This paper discusses the range-frequency distribution of the vector field due to a broadband acoustic source moving in a shallow-water waveguide as the self noise of a surface ship, and the vector extension of the waveguide impulse response measured over a limited frequency range using an active source of known waveform. From theory analysis and numerical simulation, the range-frequency representation of a vector field exhibits an interference structure qualitatively similar to that of the corresponding pressure field but, being quantitatively different, provides additional information on the waveguide, especially through the vertical component. For the range-frequency representation, physical quantities that can better exhibit the interference characteristics of the waveguide are the products of pressure and particle velocity and of the pressure and pressure gradient. An image processing method to effectively detect and isolate the individual striations from an interference structure was reviewed briefly. The representation of the vector impulse response was discussed according to two different measurement systems, also known as particle velocity and pressure gradient. The vector impulse response representation can not only provide additional information from pressure only but even more than that of the range-frequency representation.
Keywords: acoustic waveguide; vector field; range-frequency interference structure; striation processing; impulse response; normal mode
Article ID: 1671-9433(2011)04-0495-07

1 Introduction

Compared to a scalar sensor sensitive to pressure (hydrophone), a vector sensor is capable of measuring non-scalar components of the sound field, e.g., the pressure gradient and the particle velocity. A vector sensor performs collocated measurements of the scalar and vector components of the sound field and serves as a compact multichannel receiver. For equivalent performance of source localization, a vector sensor array (VSA) is more compact than a pressure-only array (Yang, 2003; Stojanovic *et al*, 1995).

Leslie (1956) gave the first derivation of mathematical expressions for a vector sensor, and showed the realization of a simple hydrophone system that can measure the water particle velocity. Some unique advantages of a vector sensor as compared to a scalar pressure sensor were indicated: high sensitivity, good directionality at low frequency, low impedance, and a low self-noise level.

Received date: 2011-10-10.
Foundation item: Supported by Office of Naval Research grant N00014-07-1-1069 , the National Nature Science Foundation of China grant 50979019 and the Belgian National Fund for Scientific Research (F.R.S. - FNRS).
***Corresponding author Email:** qunyren@ulb.ac.be
© Harbin Engineering University and Springer-Verlag Berlin Heidelberg 2011

An up-to-date and detailed introduction on vector sensors and "ocean vector acoustics" was given by Shchurov (2006). Theoretical study on processing techniques for vector field, such as the correlation technique, average acoustic intensity, and sharpening directivity, together with the results of lake experiments, were presented by Hui *et al* (2000). A preliminary study on the characteristics of an underwater sound channel for vector signal was given by Liu *et al* (2009). Because of the directionality of a vector sensor, it is usually used for source direction-of-arrival (DOA) estimation. Wong and Zoltowski (1997) proposed a method to estimate the azimuth and elevation of multiple sources with uniformly and sparsely spaced vector sensor elements. Hawkes and Nehorai (1998) examined the improvement of DOA estimation due to the higher SNR signal and directional sensitivity of VSA as compared to a pressure hydrophone array. Hawkes and Nehorai (1999, 2000, 2001, 2003) discussed the effects of sensor placement on VSA performance and presented their results on ambient noise correlation and broadband source localization. Some unique features of linear VSA in beamforming were presented by Cray and Nuttall (2001).

The possibility of using a towed VSA to form a sub-bottom profiler to replace the vertical line array of the pressure

hydrophone was discussed by Hursky and Siderius (2006). Santos *et al.* (2009) presented results on geoacoustic inversion using a vertical VSA. Osler *et al.* (2010) developed a technique to obtain the sediment speed at different frequencies by measuring the angle of refraction of an in-water sound by means of exploiting vector sensor directionality. Koch (2010) gave the principle proof and experimental results for geoacoustic inversion and source tracking with data collected on a horizontal linear VSA. Santos *et al.* (2010) discussed the use of a VSA both in DOA and bottom parameters estimation and investigated the possibility of using a small aperture VSA as an easily deployable system.

Various applications introduced above mainly make use of the higher SNR and directionality of the vector measurement as compared to pressure-only measurement. The additional waveguide information provided by a vector sensor compared to that of a scalar sensor was barely used. In this paper, the representation of the vector field is theoretically and numerically studied in term of the range-frequency distribution of received broadband sound due to a moving source such as a surface ship and the waveguide impulse response as measured with an active source of known waveform. The feasibility of using the additional vector information provided by a vector sensor for environmental characterization is discussed.

Subsequent sections are organized as follows: Section 2 introduces the interference structure of a broadband vector field in a shallow water waveguide and briefly reviews the image processing method developed for enhancing the interference structure. Section 3 discusses the extension of the scalar impulse response to the vector quantities. Conclusions are given in Section 4.

2 Interference structure in range and frequency

2.1 Interference characteristics

In a horizontal layered medium, the complex sound pressure field p generated by a point omni-directional source of circular frequency ω at depth z_0 and received at range r and depth z, can be expressed as a finite sum of normal modes (Brekhovskikh and Lysanov, 2003):

$$p(\omega,r,z)=\pi\mathrm{i}\sum_l \phi_l(z_0)\,\phi_l(z)H_0^1(\xi_l r)\approx \sum B_l\,\exp(\mathrm{i}\xi_l r)/\sqrt{r} \tag{1}$$

where $B_l=\sqrt{2\pi/k_l}\Phi_l(z_0)\Phi_l(z_0)$, Φ_l and ξ_l are the eigenfunction and eigenvalue for mode l, respectively. According to the Euler equation:

$$\rho\frac{\partial V}{\partial t}=-\nabla P \tag{2}$$

the horizontal and vertical particle velocities are, respectively:

$$V_r(\omega,r,z)=\sum_l \frac{i}{r^{3/2}\omega\rho}B_l\mathrm{e}^{\mathrm{i}\xi_l r}-\sum_l\frac{\xi_l}{\sqrt{r}\omega\rho}B_l\mathrm{e}^{\mathrm{i}\xi_l r}\approx\sum_l\frac{C_l}{\sqrt{r}}\mathrm{e}^{\mathrm{i}\xi_l r} \tag{3}$$

$$V_z(\omega,r,z)=\sum_l\frac{ik_{l,z}}{\sqrt{r}\omega\rho}B_l^l\mathrm{e}^{\mathrm{i}\xi_l r}=\sum_l\frac{D_l}{\sqrt{r}}\,\mathrm{e}^{\mathrm{i}\xi_l r} \tag{4}$$

where $C_l=\xi_l B_l/\omega\rho$, $D_l=\mathrm{i}k_{l,z}B_l'/\omega\rho$, and B_l' represents the derivative of B_l with respect to depth. The gradient of the pressure field can be also obtained from Eq.(2):

$$G_r(\omega,r,z)\approx\sum_l\frac{E_l}{\sqrt{r}}\mathrm{e}^{\mathrm{i}\xi_l r} \tag{5}$$

$$G_z(\omega,r,z)\approx\sum_l\frac{F_l}{\sqrt{r}}\mathrm{e}^{\mathrm{i}\xi_l r} \tag{6}$$

where $E_l=\xi_l B_l/\rho$ and $F_l=\mathrm{i}k_{l,z}B_l'/\rho$.

The received sound intensity, mean square values for horizontal, particle velocities and pressure gradients follow as:

$$I(\omega,r,z)\approx pp^*=\frac{1}{r}\sum_l B_l^2+\frac{1}{r}\sum_{l,m(l\neq m)}B_lB_m^*\cos\left(\Delta\xi_{l,m}r\right) \tag{7}$$

$$\left|V_r(\omega,r,z)\right|^2=V_rV_r^*=\frac{1}{r}\sum_l C_l^2+\frac{1}{r}\sum_{l,m(l\neq m)}C_lC_m^*\cos\left(\Delta\xi_{l,m}r\right) \tag{8}$$

$$\left|V_z(\omega,r,z)\right|^2=V_zV_z^*=\frac{1}{r}\sum_l D_l^2+\frac{1}{r}\sum_{l,m(l\neq m)}D_lD_m^*\cos\left(\Delta\xi_{l,m}r\right) \tag{9}$$

$$\left|G_r(\omega,r,z)\right|^2=G_rG_r^*=\frac{1}{r}\sum_l E_l^2+\frac{1}{r}\sum_{l,m(l\neq m)}E_lE_m^*\cos\left(\Delta\xi_{l,m}r\right) \tag{10}$$

$$\left|G_r(\omega,r,z)\right|^2=G_rG_r^*=\frac{1}{r}\sum_l E_l^2+\frac{1}{r}\sum_{l,m(l\neq m)}E_lE_m^*\cos\left(\Delta\xi_{l,m}r\right) \tag{11}$$

where $\Delta\xi_{l,m}=\xi_l-\xi_m$, and * denotes a complex conjugate. It should be noticed that Eqs.(7)−(11) have the same form but with different coefficients B_l, C_l, D_l, E_l and F_l, respectively. Increments of frequency $\mathrm{d}\omega$ and range $\mathrm{d}r$ in the range-frequency plane that do not change the levels of intensity, square values of particle velocities, and pressure gradients are found to satisfy:

$$\mathrm{d}I=\frac{\partial I}{\partial\omega}\mathrm{d}\omega+\frac{\partial I}{\partial r}\mathrm{d}r=0 \tag{12}$$

$$\mathrm{d}\left|V_r\right|^2=\frac{\partial\left|V_r\right|^2}{\partial\omega}\mathrm{d}\omega+\frac{\partial\left|V_r\right|^2}{\partial r}\mathrm{d}r=0 \tag{13}$$

$$\mathrm{d}\left|V_z\right|^2=\frac{\partial\left|V_z\right|^2}{\partial\omega}\mathrm{d}\omega+\frac{\partial\left|V_z\right|^2}{\partial r}\mathrm{d}z=0 \tag{14}$$

$$\mathrm{d}\left|G_r\right|^2=\frac{\partial\left|G_r^a\right|^2}{\partial\omega}\mathrm{d}\omega+\frac{\partial\left|G_r^a\right|^2}{\partial r}\mathrm{d}r=0 \tag{15}$$

$$\mathrm{d}\left|G_z\right|^2=\frac{\partial\left|G_z^a\right|^2}{\partial\omega}\mathrm{d}\omega+\frac{\partial\left|GV_z^a\right|^2}{\partial r}\mathrm{d}z=0 \tag{16}$$

The waveguide invariant was derived from Eq.(12) (Brekhovskikh and Lysanov, 2003):

$$\beta\equiv\frac{r}{\omega}\frac{\mathrm{d}\omega}{\mathrm{d}r}=\frac{\mathrm{d}(1/v)}{\mathrm{d}(1/u)}=-\left(\frac{u}{v}\right)^2\frac{\mathrm{d}v}{\mathrm{d}u} \tag{17}$$

where u and v are the average values of group and phase velocities, respectively. Since the mean square values for the particle velocities and pressure gradients have the same form with that of sound intensity, they can also be interpreted by the waveguide invariant theory.

Table 1 Typical environmental parameters for Yellow Shark environment.

Water column	Depth./m	113.1
	Thickness./m	7.5
Sediment layer	Density./ ($kg \cdot m^{-3}$)	1.5
	Sound speed./($m \cdot s^{-1}$)	1480
	Attenuation./dB	0.03
	Density./($kg \cdot m^{-3}$)	1.8
Bottom	Sound speed./($m \cdot s^{-1}$)	1530
	Attenuation./dB	0.15

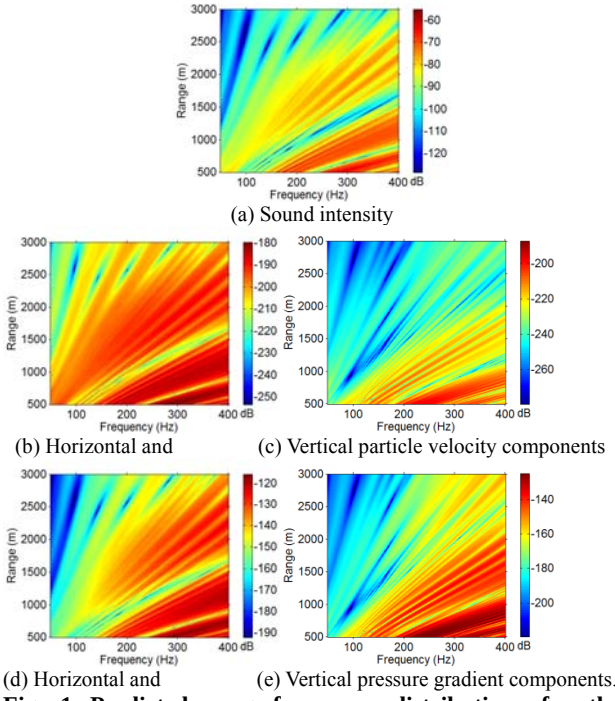

(a) Sound intensity

(b) Horizontal and (c) Vertical particle velocity components

(d) Horizontal and (e) Vertical pressure gradient components.

Fig. 1 Predicted range-frequency distributions for the Yellow Shark environment.

Figure 1 is an example of a broadband pressure field, particle velocity, and pressure gradient components for the Yellow Shark environmental model (Hermand, 1999) as calculated by the Kraken code (Porter,1997). The source and receiver depths are set to 3.5 m and 20 m, respectively. The range-frequency distributions for pressure and vector fields show similar striation structures in term of their overall trend and slope, which is in accordance with theoretical analysis: all these distributions can be interpreted by the waveguide invariant. In Fig. 1, the differences between the expressions for the vector field in Eqs.(8)–(11) and for intensity in Eq.(7) are mostly due to the eigenvalues (Eqs.(8) and (10)) and eigenfunctions (Eqs.(9) and (11)). This results in structure differences, especially for the vertical components of particle velocity or pressure gradient. Since the eigenvalues and eigenfunctions are very sensitive to environmental properties, the differences among these distributions can be taken as observable quantities to invert for environmental parameters.

2.2 Intensity flux vs particle velocity

The striations in the interference structures shown in Fig.1 are due to the coherent parts of Eqs.(7)–(11), that oscillate with range. For a hypothetical 2–mode propagation model, the distance between successive striations equal the spatial period $2\pi/\xi_1-\xi_2$. The existence of an incoherent term slowly varying in range masks the oscillatory character of the coherent term and therefore decreases the number of visible striations in the interference structure. Consequently, the mode interactions are not fully revealed by the range-frequency distributions of sound intensity, particle velocity, or pressure gradient. Finding a physical quantity that only consists of a coherent term is relevant for applications that exploit waveguide interference features. As for the pressure, since the components of particle velocity and pressure gradient consist of coherent and incoherent terms intrinsically, it is difficult to directly extract the coherent terms only. The components of intensity flux which are the products of pressure and particle velocity components are first analyzed with the aim of finding some physical quantities that only consist of coherent terms.

Following the definition of intensity flux, the real and imaginary parts of the horizontal and vertical intensity flux components are given in Eqs. (18)–(21). As the imaginary part of the horizontal intensity flux and the real part of vertical intensity flux only have coherent terms (see Eqs. (19) and (20)), they better exhibit the waveguide interference characteristics. More striations are expected to appear along range at a given frequency in their range-frequency distributions than for the intensity and particle velocity components.

$$\mathrm{real}(F_r) \approx -\frac{\sum_l \xi_l B_l B_l^*}{r\omega\rho} + \sum_{l,m(l\neq m} \xi_m B_l B_m^* \cos\left[r(\xi_l - \xi_m)\right] / 2r\omega\rho \tag{18}$$

$$\mathrm{imag}(F_r) \approx -\sum_{l,m(l\neq m} \xi_m B_l B_m^* \sin\left[r(\xi_l - \xi_m)\right] / 2r\omega\rho \tag{19}$$

$$\mathrm{real}(F_z) \approx \sum_{l,m(l\neq m} \frac{k_{m,z} B_l \left(B_m^{'}\right)^* \sin\left[r(\xi_l - \xi_m)\right]}{2r\omega\rho} \tag{20}$$

$$\mathrm{imag}(F_z) \approx -\frac{\sum_l \xi_{l,z} B_l \left(B_l^{'}\right)^*}{r\omega\rho} + \sum_{l,m(l\neq m} \frac{\xi_m B_l \left(B_m^{'}\right)^* \cos\left[r(\xi_l - \xi_m)\right]}{2r\omega\rho} \tag{21}$$

Fig.2 shows an example of the imaginary part of horizontal intensity flux and real part of vertical intensity flux for the Yellow Shark environment. Comparison with Fig.1 shows more striations than for pressure and particle velocities, especially at low frequencies. Similar quantities that can better exhibit the waveguide interference structure are the

products of pressure and pressure gradient for the imaginary part of the horizontal component and the real part of the vertical component (not shown here).

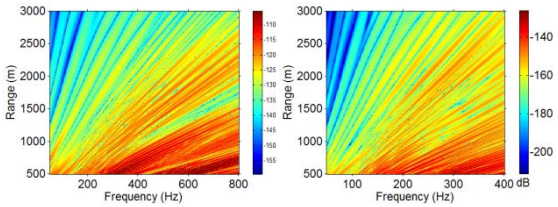

(a) (b)

(a) Imaginary part of horizontal intensity flux;
(b) Real part of vertical intensity flux.

Fig.2 Range-frequency distribution of intensity flux components.

2.3 Striation processing

A multi-scale (Frangi *et al*, 1998) line filter was adopted for processing the striations (Ren *et al*, 2011), whose output is maximized at the scale that approximately matches the line width:

$$V = \max_{\sigma_{\min} \le \sigma \le \sigma_{\max}} V_\sigma \tag{22}$$

where $\sigma_{\min}$ and $\sigma_{\max}$ are the minimum and maximum of the scales between which relevant linear structures are expected to be found; V_σ is the filter response at a fixed scale. The results of filtering the sound field distributions in Fig. 1 are shown in Fig. 3.

The original interference structures are greatly enhanced. Most striations are detected and identified as separate lines. The striation pattern difference (e.g., striation position and number) between the pressure field and vertical component of the vector field can be seen more clearly. More lines are detected for the intensity flux components than for the pressure, particle velocity, and pressure gradient fields.

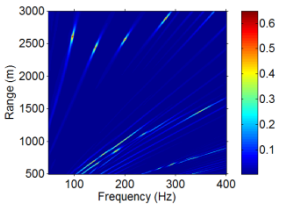

(a) sound intensity

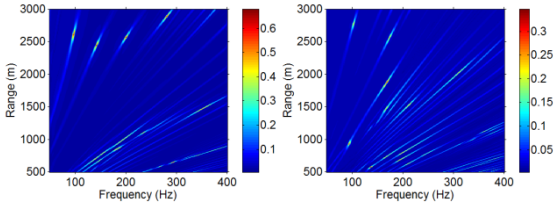

(b) horizontal and (c) vertical particle velocity components

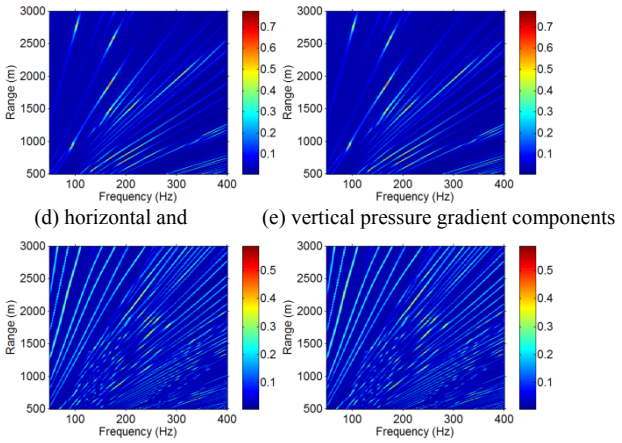

(d) horizontal and (e) vertical pressure gradient components

(f) Imaginary part of horizontal intensity flux; (g) Real part of vertical intensity flux.

Fig.3 Calculated line structures of the range-frequency distributions

3 Vector impulse response

The model-based matched filter (MBMF) has been shown to be an effective processor in inverting for geoacoustic properties in shallow water environments (Hermand, 1999) The fully phase-coherent processor is based on prediction of the scalar (pressure) impulse response of the waveguide and, being fully phase-coherent, exploits its detailed characteristics. Its extension to vector quantities is considered here. The aim is to improve the performance of compact and sparse array used for environmental characterization (Hermand and Le Gac, 2008)

A time-domain pressure signal is usually obtained by Fourier synthesis (Jensen et al, 1994):

$$p(t) = \mathrm{FFT}^{-1}(P(\omega)) = \frac{1}{2\pi}\int_{-\infty}^{\infty} S(\omega)P(\omega)\mathrm{e}^{-\mathrm{j}\omega t}\mathrm{d}\omega \tag{23}$$

where $S(\omega)$ is the source spectrum, and $P(\omega)$ is the complex CW pressure solution provided by a propagation model. Assuming a harmonic source signal, the particle velocity can be obtained by Eq. (2):

$$V(\omega) = -\frac{1}{\mathrm{i}\omega\rho}\nabla P(\omega) \tag{24}$$

Similar with that of the pressure signal, the time-domain particle velocity signal is:

$$v(t) = \mathrm{FFT}^{-1}\left(V(\omega)\right) \tag{25}$$

Usually, one uses a finite difference method to get particle velocity, considering a central difference:

$$V_r(r,z,\omega) = -\frac{p(r+\mathrm{d}r,z,\omega) - p(r-\mathrm{d}r,z,\omega)}{2\mathrm{i}\omega\rho\mathrm{d}r} \tag{26}$$

$$V_z(r,z,\omega) = -\frac{p(r+\mathrm{d}z,\omega) - p(r-\mathrm{d}z,\omega)}{2\mathrm{i}\omega\rho\mathrm{d}z} \tag{27}$$

where $\mathrm{d}r$ and $\mathrm{d}z$ are the horizontal and vertical displacements, respectively.

For the numerical simulations in this section, the depths of

the source and receiver were both set to 110 m and the displacements dr and dz were both set to 10 cm. The range between the source and receiver was set to 9 km. Figures 4(a)−4(c) show the impulse response of the waveguide over a frequency range of 200─600Hz. An increment of Δf = 4Hz was used in calculating the complex CW pressure solutions. As for the range-frequency representation, the responses for pressure and horizontal particle velocity show essentially the same arrival structure (except for a phase reversal), with a correlation coefficient of 0.996 between them. The pressure and vertical particle velocity component shows a much stronger difference, with a much smaller correlation coefficient of 0.335. This suggests that the horizontal component of particle velocity can at least provide a higher SNR waveguide impulse response, while the vertical component can provide additional information on the waveguide. Such advantages are therefore expected to improve the performance of model-based matched filter applications compared with those using only the pressure response.

The plane-wave *impedance relationship* (Jensen *et al.*, 1994) between pressure and particle velocity is used here to validate the simulation results:

$$\frac{p}{v} = \rho c \tag{28}$$

where ρ and c are the density and sound speed of the waveguide, respectively. The excellent match between the envelopes of $P/\rho c$ and $\sqrt{v_r^2 + v_Z^2}$ in Fig.4(d) shows that the *impedance relationship* is well satisfied and indicates the accuracy of the calculation.

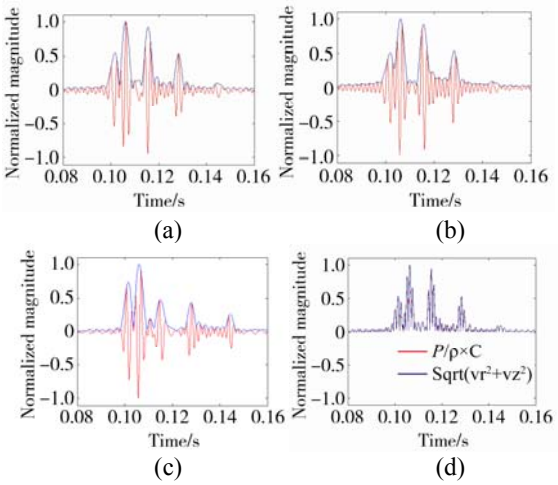

Fig. 4 Waveguide impulse response (red) and envelope (blue) for (a) pressure and (b) horizontal and (c) vertical particle velocity components. (d) Illustration of the impedance relation between the instantaneous pressure and particle velocity modulus.

The pressure-gradient vector sensor is also commonly used in underwater acoustics, which employs a finite-difference approximation of the pressure field to estimate the pressure field gradient. The following section discusses two different methods to predict the waveguide impulse response of the pressure gradient components.

First, one can also use the IFFT to get the time-domain pressure gradient from a complex sound field:

$$g(t) = \mathrm{FFT}^{-1}(G(\omega)) \tag{29}$$

Second, similar to the principle of gradient vector sensor measurement, the time-domain pressure gradient can be directly obtained from the time-domain pressure:

$$g_z(r,z,t) = -\frac{p(r,z+\mathrm{d}z,t) - p(r,z-\mathrm{d}z,t)}{2\rho \mathrm{d}z} \tag{30}$$

$$g_r(r,z,t) = -\frac{p(r+\mathrm{d}r,z,t) - p(r,z-\mathrm{d}r,z,t)}{2\rho \mathrm{d}r} \tag{31}$$

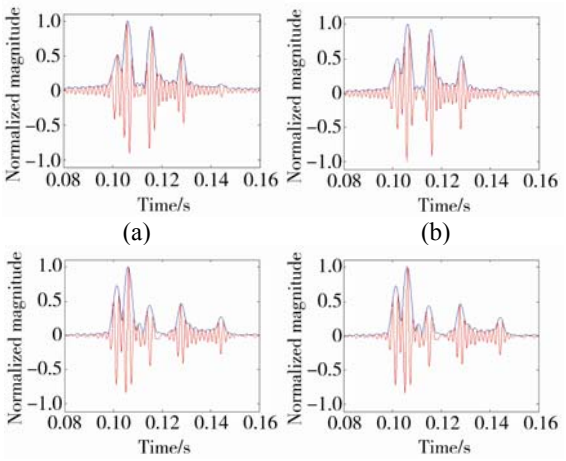

Fig. 5 Waveguide impulse response (red) and envelope (blue) obtained by the inverse Fourier transform for (a) horizontal and (c) vertical pressure gradients and by direct finite difference for (b) horizontal and (d) vertical pressure gradients.

Fig.5 compares the impulse response and envelope of the pressure gradient for the two calculation methods. For both horizontal and vertical components the respective numerical results are identical. One or the other method can be conveniently chosen according to the forward model used. Comparison with Fig. 4(a) shows that not only the vertical component of the pressure gradient but also the horizontal component has a different structure than that of pressure. Both components can provide additional information on the waveguide compared with information from the pressure. Therefore, the use of a pressure-gradient vector sensor and MBMF processing of the two-component signal are expected to further improve the inversion results compared to results from a particle-velocity vector sensor that only provides additional environmental information through its vertical component signal.

4 Conclusions

For the representation in the range-frequency domain, the

vector field exhibits an interference structure similar to that of a pressure field, but typically with a different set of striations, especially for the vertical component. Differences such as the position and slope of the striations are characteristics of the environment and can therefore be used in an inversion scheme for environmental characterization. Furthermore, an increased number of deeper striations can be obtained by the product of pressure and particle velocity components (or pressure gradient), which better represent the interference characteristics of broadband sound propagation. With regard to interference structure processing, a multi-scale version of the line filter is shown to be an effective tool in striation detection and isolation. The calculation of a band-limited waveguide impulse response was derived for two types of vector sensor output: particle velocity and pressure gradient. The temporal structure of the vertical component of particle velocity markedly differs from that of pressure. On the other hand, for the pressure gradient, both horizontal and vertical components show differences in their structure compared to that of pressure. These simulation results suggest that the vector impulse response can provide more information on the waveguide acoustic properties and is expected to improve the inversion for environmental parameters.

Acknowledgement

Work supported by Office of Naval Research grant and the National Natural Science Foundation of China. The author Qun-yan Ren would like to acknowledge the Belgian National Fund for Scientific Research (F.R.S. - FNRS) for supporting the research.

References

Brekhovskikh LM, Lysanov YP (2003). *Fundamentals of Ocean Acoustics*. Springer, 3rd edition.

Chuprov, SD (1982). Interference structure of a sound field in a layered ocean. Acoustics of the Ocean: Current Status, 71–91. (in Russian)

Cray BA, Nuttall AH (2001). Directivity factors for linear arrays of velocity sensors. *J. Acoust. Soc. Am*., **110**(1), 324–331.

Frangi AF, Niessen WJ, Vincken KL, Viergever MA (1998). Multiscale vessel enhancement filtering. *Medical Image Computing and Computer-Assisted Interventation*.

Hawkes M, Nehorai A (1998). Acoustic vector-sensor beamforming and Capon direction estimation. *IEEE J. Oceanic Eng.*, **46**(9), 2291–2304.

Hawkes M, Nehorai A (1999). Effects of sensor placement on acoustic vector sensor array performance. *IEEE J. Oceanic Eng.*, **24**(1), 33–40.

Hawkes M, Nehorai A (2000). Acoustic vector-sensor processing in the presence of a reflecting boundary. *IEEE Transactions on Signal Processing*, **48**(11), 2981–2993.

Hawkes M, Nehorai A (2001). Effects of sensor placement on acoustic vector sensor array performance. *IEEE J. Oceanic Eng.*, **24**(1), 33–40.

Hawkes M, Nehorai A (2003). Wideband source localization using a distributed acoustic vector-sensor array. *IEEE Transactions on Signal Processing*, **51**(6), 1479–1491.

Hermand JP and Le Gac JC (2008). Subseafloor geoacoustic characterization in the kilohertz regime with a broadband source and a 4-element receiver array. *Proc. OCEANS '08*, Quebec City, QC.

Hermand JP (1999). Broad-band geoacoustic inversion in shallow water from waveguide impulse response measurements on a single hydrophone: theory and experimental results. *IEEE J. Oceanic Eng*., **24**(1), 41–66.

Hui JY, Hui L, Yu HB, Fan MY (2000). Study on the physical basis of pressure and particle velocity combined processing. *Acta Acustica*, **4**, 303–307.

Hursky P, Siderius M (2006). Using ambient noise and vector sensor arrays to form a subbottom profiler. *J. Acoust. Soc. Am.*, **120**(1), 3027.

Jensen FB, Kuperman WA, Porter MB, Schmidt H (1994). *Computational Ocean Acoustics (Modern Acoustics and Signal Processing)*, American Institute of Physics.

Koch RA (2010). Proof of principle for inversion of vector sensor array data. *J. Acoust. Soc. Am*., **128**(2), 590–599.

Leslie CB (1956). Hydrophone for measuring particle velocity. *J. Acoust. Soc. Am.*, **28**(4), 711–715.

Lindeberg Y (1996). Edge detection and ridge detection with automatic scale selection. *In Conf. on Comp. Vis. and Pat. Recog*.

Liu W, Li Y, Piao SC (2009). Study on correlation processing for acoustic vector signals in underwater sound channel. *The 10th Western Pacific Acoustics Conference*, Beijing, China.

Osler JC, Chapman DMF, Hines PC (2010). Measurement and modeling of seabed particle motion using buried vector sensors. *IEEE J. Oceanic Eng*., **35**(3), 516–537.

Petnikov VG, Kuz'kin K (2002). Shallow water variability and its manifestation in the interference pattern of sound fields. *AIP Conference Proceedings*, 207–217.

Porter (1997). The KRAKEN normal mode program. http://oalib.hlsresearch.com/Modes/AcousticsToolbox/manual_html/kraken.html [available online].

Ren QY, Hermand JP, and Piao SC (2011). The interference phenomena of the broad-band vector field and striation processing. *4th Underwater Acoustic measurements: Techniques and Results*, Greece

Santos P, Rodriguez OC, Felisberto P, Jesus SM, Faro P (2009). Geoacoustic matched-field inversion using a vertical vector sensor array. *3rd International Conference and Exhibition on Underwater Acoustic Measurements Technologies and Results*., Greece.

Santos P, Felisberto P, Jesus SM (2010). Vector sensor arrays in underwater acoustic applications. *Emerging Trends in Technological Innovation: First IFIP WG 5.5/SOCOLNET Doctoral Conference on Computing, Electrical and Industrial Systems*, DoCEIS 2010, Costa de Caparica, Portugal.

Shchurov VA (2006). *Vector acoustics of the ocean*. Vladivostk: Dalhauka.

Stojanovic M, Catipovic JA, Proakis JG (1995). Reduced-complexity spatial and temporal processing of underwater acoustic communication signals. *J. Acoust. Soc. Am.*, **98**, 961–972.

Wong KT, Zoltowski MD (1997). Extended-aperture underwater acoustic multisource azimuth/elevation direction-finding using uniformly but sparsely spaced vector hydrophones. *IEEE J. Oceanic Eng.*, **22**(4), 659-672.

Yang TC (2003).Temporal resolutions of time-reversal and passive phase conjugation for underwater acoustic communications. *IEEE J. Oceanic Eng*., **28**, 229-245.

Qunyan Ren received his undergraduate diploma in Electronic and Information Engineering and a masters degree in Underwater Acoustics Engineering, both from Harbin Engineering University (HEU) in 2006 and 2009, respectively. He is currently a PhD student at the Environmental Hydroacoustics Laboratory, Faculty of Applied Science, Université libre de Bruxelles (U.L.B.), Belgium, in co-tutelle with the National Key Laboratory of Underwater Acoustic Technology, HEU, China, under the co-supervision of Prof. Jean-Pierre Hermand and Prof. Sheng-chun Piao from U.L.B and HEU, respectively. His research interests are underwater sound propagation, signal processing and geoacoustic inversion. His PhD research work focus on the development of passive interferometry technique to process the broadband ship noise field measured by vector sensors for the characterization of shallow water environments.

Jean Pierre Hermand received a Ingénieur Civil degree in electrical and mechanical engineering and a PhD degree in applied sciences from the Université libre de Bruxelles (U.L.B.), Belgium.

Currently, he is a professor and research director at U.L.B., where he founded the Environmental Hydroacoustics Laboratory (EHL) in 2001. He coordinates ocean acoustics research and fieldwork in the framework of European and international projects. His current research interests include adjoint modeling and sequential Bayesian filtering for geoacoustic inversion, and the integrated use of active and passive acoustics to remotely sense and characterize very shallow aquatic ocean environments, and in particular, marine habitats and river sediment dynamics.

Dr. Hermand is a fellow of the IEEE and a fellow of the Acoustical Society of America (ASA). He is currently the IEEE Chair of the OES Technical Committee on Ocean Signal and Image Processing. He is a member of the administrative committee of the IEEE Oceanic Engineering Society.

Shengchun Piao received a PhD degree from Harbin Engineering University, China. Currently, he is a professor and research director at the College of Underwater Acoustic Engineering in Harbin Engineering University. His current research interests include underwater sound propagation modeling and ocean acoustics, such as geoacoustic inversion.